Application of second near infrared fluorescence imaging to trace CelTrac1000-labeled hair follicle epidermal neural crest stem cells in repairing rat facial nerve defects

Shangrui Lv

Nanjing Medical University Affiliated Wuxi No.2 People's Hospital: Wuxi No 2 People's Hospital

Guochen Zhu (✉ zgc2003doctor@njmu.edu.cn)

Nanjing Medical University Affiliated Wuxi No.2 People's Hospital: Wuxi No 2 People's Hospital

https://orcid.org/0000-0003-4814-1550

Jing Zhang

Nantong University affiliated Wuxi Clinical College

Li Tang

Nanjing Medical University Affiliated Wuxi No.2 People's Hospital: Wuxi No 2 People's Hospital

Qiong Li

Nanjing Medical University Affiliated Wuxi No.2 People's Hospital: Wuxi No 2 People's Hospital

Research Article

Abstract

Background Tissue engineering based on stem cells has achieved satisfactory results in repairing facial nerve defects. However, the *in vivo* process of the transplanted cells has not been fully clear until now, although it is critical to understand the process and the underlying mechanism of regeneration for better therapeutic outcomes. Recently, second near-infrared window (NIR-II) fluorescence imaging has emerged as a rapidly evolving bio-imaging technique capable of visualizing and quantifying biological processes at the cellular level of living organisms.

Methods Firstly, rat hair follicle epidermal neural crest stem cells (EPI-NCSCs) were isolated, cultured and identified by expression of SOX10 and Nestin, and then labeled with CelTrac1000. Rat acellular nerve allografts (ANAs) were prepared by chemical extraction. Secondly, 30 adult male rats were randomly and equally assigned into three groups: ANA + cells group, ANA group, and autograft group. The buccal branch of the facial nerve on right side was exposed and a 10-mm-long gap was bridged by ANA laden with CelTrac1000-labeled EPI-NCSCs, ANA laden with CelTrac1000 dye, and autologous nerve, respectively. Thirdly, CelTrac1000-labeled EPI-NCSCs were detected by NIR-II optical imaging system to visualize the behavior of the transplanted cells *in vivo* postoperatively. Finally, vibrissa movement, compound muscle action potentials (CMAPs) of vibrissal muscle, facial motoneurons retrotraced by Fluorogold, morphology and histology of the regenerated nerves in three groups were analyzed after surgery, respectively.

Results Through 14 weeks of dynamic observation, we found that EPI-NCSCs successfully survived in the ANAs *in vivo*. Meanwhile, the region of the NIR-II fluorescence signals was gradually limited to be consistent with the route of the regenerative segment of the facial nerve. Furthermore, the degree of the vibrissa movement, the recovery value of the onset latency and amplitude of CMAPs, the number of Fluorogold-labeled cells, the CD31 positive area/total area, the mean gray value of S100 and β-tubulin III, the number and the diameter of the myelinated nerve fibers in the ANA group were lower than the other two groups ($P < 0.05$), and the other two groups had similar values ($P > 0.05$). Additionally, the thickness of the myelin sheaths was the thinnest in the ANA group, and the thickest in the autograft group ($P < 0.05$).

Conclusions The migration map of local CelTrac1000-labeled EPI-NCSCs was successfully monitored by the NIR-II fluorescence imaging system when EPI-NCSCs within the ANAs were applied to treat rat facial nerve defects. Additionally, EPI-NCSCs promoted the ANAs to repair facial nerve defects in a small animal model.

1. Introduction

For promoting neural regeneration, tissue engineering based on implantation of autologous or allogeneic stem cells is considered as a promising repair scheme [1–4]. However, some reports suggested that the survivability of stem cells might be hampered by rejection, inflammation, or migration *in vivo* after

implantation [5–7]. Therefore, there is an urgent demand for non-invasive imaging techniques that can monitor the fate of the transplanted cells *in vivo* to further elucidate the role of stem cells in neuro-regenerative medicine. Through imaging examinations such as magnetic resonance imaging, single-photon emission computed tomography, and positron emission tomography/computed tomography, direct labeling strategies possess the advantages of abundant cell trackers and minimal interference to the transplanted cells [8–12]. In practice, the cell tracking methods described above have their drawbacks, such as being expensive, and limited temporospatial resolution. In 2019, Rbia applied luciferase-based bioluminescence imaging to detect adipose-derived mesenchymal stromal cells within nerve allografts, and found that the implanted cells could survive after surgery, but the detectable period was limited *in vivo* [13, 14]. Additionally, some studies suggested that green fluorescent protein-transfected cells could emit green fluorescence with the assistance of the *in vivo* imaging systems, although most studies of green fluorescent protein-labeled cells after transplantation have so far been limited to tissue sections [15]. Since 2019, the exploration of the second near-infrared window (NIR-II; 1,000–1,700 nm) optical imaging system, and the development and utilization of new fluorescent probes have driven advances in real-time visualization and monitoring of post-transplant stem cells *in vivo* [16, 17]. NIR-II optical imaging system can detect tissue at depths of centimeters and achieve micron resolution at millimeter depths. Chen reported that a novel NIR-II probe, CelTrac1000, could efficiently label stem cells within a few hours, accumulate in the cytoplasm of cells after absorption, with minimal leakage and interference to cell functions [18]. CelTrac1000 consisted of an equal concentration of CH-4T and Tat-HSA, the former was a synthetic organic NIR-II dye and the latter was composed of human serum albumin (HSA) conjugated with a cell-penetrating peptide from the transcriptional activator protein (Tat). CelTrac1000 has the advantages of well-defined components, high purity, low cytotoxicity, and high temporospatial resolution. However, the application of NIR-II and CelTrac1000 in the detection of exogenous stem cells after peripheral nerve defect has not been reported so far [19].

Since 2013, hair follicle epidermal neural crest stem cells (EPI-NCSCs) have been regarded as a sort of ideal seed cells due to their wide distribution, easy access, and biological properties of expressing a variety of neurotrophic factors, extracellular proteases, and vascular factors in central or peripheral nerve injury [20–22]. Similar to other stem cells, knowledge of the survival rate of the transplanted EPI-NCSCs and the efficiency of EPI-NCSCs differentiation into functional neuronal cells *in vivo* are the most important key-points related to research on neuro-regenerative medicine, and thus accelerate the clinical application of stem cell therapy [23]. Inspired by the development and utilization of NIR-II and CelTrac1000, we proposed that cells labeled with CelTrac1000 and monitored by NIR-II imaging techniques may be applied in evaluating the behavior of the transplanted cells when they are used to repair peripheral nerve injury.

In the present study, CelTrac1000-labeled EPI-NCSCs were micro-injected into the acellular nerve allografts (ANAs) to bridge the 10-mm defect of the rat facial nerve [24, 25]. Then, we traced CelTrac1000-labeled EPI-NCSCs by NIR-II optical imaging system, and obtained a temporospatial map of the behavior of EPI-NCSCs *in vivo* for up to 14 weeks. Meanwhile, the correlation between such characters and the

facial nerve regeneration effect was further verified by functional test and histological observation in the ANA-laden with EPI-NCSCs group, compared with the cell-free ANA group and autograft group.

2. Materials and methods

2.1 Animals

Thirty-five adult male Sprague-Dawley (SD) rats (weighing 270-330g; eight to nine weeks old) were purchased from the specific pathogen-free laboratory of the Animal Laboratory Center at the Key Laboratory on Technology for Jiangsu Institute of Parasitic Diseases, China (SYXK-Su-2019-0025). Five rats were used to prepare EPI-NCSCs and ANAs, and the other 30 rats were applied to bridge facial nerve defects *in vivo*, respectively. All rats were maintained at (22 ± 1)°C room temperature with a 12/12 hour light/dark cycle and had free access to food and water. All animal experiments were conducted according to the ARRIVE (Animals in research: reporting in vivo experiments) guidelines, and approved by the Laboratory Animal Management Committee and the Ethics Review Committee of Nanjing Medical University Affiliated with Wuxi No 2 People's Hospital (approval No. 2018-D-1) on March 15, 2018.

2.2 Isolation, culture and identification of EPI-NCSCs

Two rats were anesthetized with 3% sodium pentobarbital (30 mg/kg; Sigma-Aldrich, USA) by intraperitoneal injection. After separated from the surrounding tissue, the bulges of the vibrissal hair follicles were harvested, and then inoculated in the culture dish which was pre-coated with rat tail collagen I and rinsed with the culture medium before inoculation. The culture medium contained Dulbecco's Modified Eagle Media/Ham's F 12 nutrient medium (DMEM/F12, LABGIC, Beijing, China), 10% (v/v) fetal bovine serum (FBS, Thermo Fisher Scientific, MA, USA), 2% B27 NeuroMix (Thermo Fisher Scientific, MA, USA), 1% N2 supplement (Thermo Fisher Scientific, MA, USA), 0.025% Insulin-Transferrin-Selenium (ITS) Media Supplement (Sigma-Aldrich, USA), 20 ng/mL basic fibroblast growth factor (bFGF, PeproTech (Suzhou), Jiangsu, China), 20 ng/mL epidermal growth factor (EGF, PeproTech (Suzhou), Jiangsu, China), 200 mM L-glutamic acid (Thermo Fisher Scientific, MA, USA). Next, the explants were cultured at 37°C and 5% CO_2 for 2−3 hours in order for them to be attached to the bottom wall of the plates. Then, 3 mL culture medium was added into the plates, and the explants were cultured at the same condition for 10 days until a few cells were emigrated out of hair follicular bulges. Finally, cells were further cultured for 5 days after the explants were discarded. The culture medium was changed every 3 days. The cells were passaged when they reached 90% confluence.

According to our previous report, cells were identified by immunofluorescent cytochemical staining of Anti-SOX10 antibody (1:100, Abcam, Cambridge, UK) and Anti-Nestin antibody (1:100, Abcam, Cambridge, UK), respectively [22]. Subsequently, Cy3 Goat Anti-Rabbit IgG (H + L) (1:100, Servicebio, Hubei, China) and Cy3 Goat Anti-Mouse IgG (H + L) (1:100, Servicebio, Hubei, China) were incubated at 37°C for 1 hour without light. Finally, cells were observed under an inverted fluorescence microscope (OLYMPUS IX71, Japan).

2.3 Preparation of CelTrac1000

Tat-HSA and CH-4T were provided by the Center for Molecular Imaging Research, Shanghai Institute of Medical Material, Chinese Academy of Sciences. The synthesis protocol of CelTrac1000 was based on Chen's report: 13.6 mg of Tat-HSA and 0.28 mg CH-4T were dissolved in 1 × phosphate buffer saline (0.2 mL) [18]. The mixture was treated with ultrasound (120 watts) for 30 minutes to manufacture 1mM CelTrac1000 solution (0.2 mL).

2.4 EPI-NCSCs labeled by CelTrac1000

When rat EPI-NCSCs reached 80% confluence, the medium was replaced with 2 mL fresh medium and 100 μL CelTrac1000 solution (the final concentration of Celtrac1000 was 50 μM), and the mixture was then co-cultured for 12 hours [18]. Then, mixture was trypsinized and collected, centrifuged at 1000 revolutions per minute for 3 minutes. After that, the supernatant liquid was removed, and the precipitate was re-suspended by cell medium to make a single-cell suspension for the subsequent experiment.

Part of single-cell suspension was diluted with 0.4% trypan blue solution (Solarbio, Beijing, China), and the viability of Celtrac1000-labeled EPI-NCSCs was more than 90%, indicating that the NIR-II dye was safe and had no obvious effect on the cell viability.

2.5 Construction of nerve transplantation

ANAs were prepared by chemical extraction of the Sondell's scheme and our slight modification from the tibial nerves of 5 adult rats [24, 25]. In the ANA + cells group, 10 μL of CelTrac1000-labeled EPI-NCSCs with concentration of 5×10^7 cells/mL was micro-injected into the 10-mm-long ANAs from one end. Similarly, 10 μL of CelTrac1000 dye solution without cells was micro-injected into the ANAs in the ANA group.

2.6 Rat surgical model of facial nerve defect and repair

In the *in vivo* part of the experiment, 30 rats were randomly and equally assigned into three groups according to the completely randomized design: ANA + cells group, ANA group, and autograft group. After deep anesthesia as mentioned in 2.2, the buccal branch of the facial nerve on right side was exposed and an 8-mm-long segment was harvested, then a gap of 10 mm occurred when the stumps were retracted. Meanwhile, in order to eliminate the influence of the marginal mandibular branch of the facial nerve on the recovery of vibrissa movement, a 10-mm-long segment of the marginal mandibular branch was transected in all groups [26]. Finally, the gap was bridged by ANA laden with CelTrac1000-labeled EPI-NCSCs, ANA laden with CelTrac1000 dye, and autologous marginal mandibular branch of the facial nerve, respectively. All procedures were performed under an Olympus operating microscope (Olympus, Japan). After surgery, animals were housed in a standard environment and monitored daily for signs of infection and/or distress. At the appropriate endpoints, animals were euthanized by anesthesia overdose, and the regenerative nerves were collected for further studies.

2.7 *In vivo* imaging

After transplantation, the activity tracking of exogenous cells in the scaffolds was non-invasively monitored based on an 808-nm fluorescence signal for up to 14 weeks (1w, 2w, 3w, 6w, 9w and 14w). Real-time NIR-II fluorescence images were recorded by a customized NIR-II small animal imaging facility (Princeton Instruments, NIRvana TE 640, USA). First, six rats were randomly selected from ANA + cells group (n = 3) and ANA group (n = 3), and anesthetized with 29% O_2 mixed with 3% isoflurane. Then, rats were placed on In Vivo NIR-II Optical Imaging System (MARS, Shanghai, china) with the left side-lying position. The parameters for photo acquisition were selected as mentioned in Chen's report [18]. Finally, the obtained images were processed and analyzed with Image J (National Institutes of Health, USA).

2.8 Vibrissa movement and neuromyography

The vibrissa movement of 24 rats (8 rats per group) was evaluated every 2 weeks after surgery. A scale of 0–4 was used to describe and analyze the vibrissa movement of the right side: 0 for no movement, 1 for mild movement, 2 for mild to moderate movement, 3 for obvious but asymmetrical movement, and 4 for symmetrical movement.

Fifteen rats were randomly selected from the three groups (5 rats per group), and compound muscle action potentials (CMAPs) of vibrissal muscle on both sides were recorded by an electromyograph and evoked potential equipment (Keypoint 4, Medtronic Corporation, USA). Finally, the recovery ratios of onset latency and amplitude of CMAPs were calculated by dividing the values of the surgical side by the values of the contralateral side.

2.9 Facial motoneurons retrotraced by Fluorogold

Twelve rats were randomly selected from three groups (4 rats per group), and 5 μL of 5% Fluorogold (US UElandy Inc., Jiangsu, China) was micro-injected into the distal portion of the nerve graft. Five days later, the rats were fixed with 4% paraformaldehyde solution after general anesthesia as mentioned in 2.2. Then, brainstems were removed and dehydrated gradiently with sucrose solution for another 3 days. Next, brainstems were cross-sectioned by a Leica freezing microtome (LEICA CM1950, Wetzlar, Germany), and the thickness of the frozen slices was 10 μm. Finally, the sections were observed by an inverted fluorescence microscope (OLYMPUS IX71, Olympus, Japan), and the total number of the labeled neurons was calculated by counting at intervals of 50 μm.

2.10 Morphological observation and histological analysis of the regenerated nerves

At 14 weeks postoperatively, the morphology of the regenerated nerves in the three groups was observed and measured under an Olympus operating microscope (Olympus, Japan). Then, the regenerative nerves were harvested for the histological analysis.

Some segments of three rats from each group were fixed in 2.5% glutaraldehyde solution for 8 hours and postfixed in 1% osmium tetroxide for 2 hours, and embedded in epoxy resin. Next, the ultra-thin sections (70 nm) were double stained with 2% uranyl acetate (Sigma, USA) and lead stain (Sigma, USA) solution,

and examined by a transmission electron microscope (HT7700, Hitachi, Japan) at a magnification of 1200 folds. Six randomly selected fields were captured for each section from each group to assess the number and the diameter of the myelinated nerve fibers, and myelin sheath thickness [27].

Others were fixed in 4% neutral paraformaldehyde and embedded in paraffin to perform CD31, soluble protein-100 (S100) and β-tubulin III immunofluorescent staining [28]. Firstly, sections were treated with antigen retrieval solution (citrate buffer, pH 6.0; Sigma, USA) at 96℃ for 5 minutes, blocked with 10% goat serum (Boster, Hubei, China). Then, sections were immunolabeled with primary antibodies CD31 (Rabbit monoclonal IgG; 1:200; Santa Cruz, USA), S100 (Rabbit monoclonal IgG; 1:100; Abcam, UK) and β-tubulin III (Mouse monoclonal IgG; 1:500; Abcam, UK) to label neovessels, Schwann cells and axons, respectively. Positively immunofluorescent markers were visualized by incubation with Cy3-conjugated Affinipure Goat Anti-Mouse IgG (H + L) (1:200, Proteintech, UK), FITC-conjugated anti-rabbit secondary antibody (Goat Polyclonal IgG; 1:50; ZF-0311, ZSGB-BIO, Beijing, China) and TRITC-conjugated anti-mouse secondary antibody (Goat Polyclonal IgG; 1:50; ZF-0313, ZSGB-BIO, Beijing, China), respectively. Finally, images were captured under an Olympus IX73 microscope (Olympus, Japan) and analyzed with Image J (National Institutes of Health, USA).

2.11 Statistical analysis

All the calculation, statistical analyses, and graphs were performed by GraphPad Prism 9.4.1 (GraphPad Software Inc., USA) and SPSS 24.0 Software (IBM, Armonk, NY, USA). All data were expressed as mean ± standard error of the mean, and analyzed by one-way analysis of variance (ANOVA), two-way ANOVA, and repeated measurement ANOVA. Bartlett's test was performed to check the homogeneity test of variance, and Tukey *Post hoc* test was made only if F had a $p < 0.05$ and no significant variance inhomogeneity was found within the analysed groups. Statistical significance levels were indicated as follows: * $P < 0.05$, ** $P < 0.01$, *** $P < 0.001$, **** $P < 0.0001$. $P < 0.05$ indicated a statistically significant difference.

3. Results

3.1 Identification of rat EPI-NCSCs

After 10 days of culture, a few spindle-shaped cells were scattered on the bottom wall of culture plates (Fig. 1A). With the extension of cell culture days, the number of cells gradually increased. As shown in Fig. 1B-D, cells were positively expressed for SOX10 (a marker of neuroectodermal stem cells) and Nestin (a marker of neural stem cells), respectively.

3.2 Real-Time and dynamic NIR-II fluorescence imaging of EPI-NCSCs *in vivo*

In the ANA + cells group, strong NIR-II fluorescence signals with scattered, irregular shape were observed in the operative area centered on the graft segment during the first 3 weeks after surgery (Fig. 2A-C). From then on, the region of the NIR-II fluorescence signals was gradually limited, and tended to be consistent

with the direction of the buccal branch of the facial nerve (Fig. 2D-F). In the ANA group, weak NIR-II fluorescence signals were observed in the operative area from one week to two weeks after surgery, and no fluorescence signal was detected since the 3rd week (not shown).

To semiquantitatively evaluate the migration and proliferation of the exogenous EPI-NCSCs in the ANA + cells group, the fluorescence area and the average fluorescence intensity of the area were measured in the fluorescence region. As shown in Fig. 3, the average fluorescence intensity did not fluctuate significantly during the observation period, though the fluorescence area tended to be limited in the grafts.

3.2 Functional assessment

The vibrissa movement of rats on the injured side recovered gradually in all groups. The degree of the vibrissa movement in the ANA group was worse than that in the other two groups ($P < 0.05$), while there was no significant difference in the degree of the vibrissa movement between the ANA + cells group and the autograft group at each time point ($P > 0.05$) (Fig. 4).

CMAPs were recorded on the injured side at 14 weeks postoperatively. The recovery value of the onset latency and amplitude of CMAPs in the ANA group was worse than that in the other two groups ($P < 0.05$), while the recovery value of the onset latency and amplitude of CMAPs in the ANA + cells group was similar to that in the autograft group ($P > 0.05$) (Fig. 5).

3.3 Fluorogold-labeled facial motoneurons

Labeled cells with irregular shape or multipolar neurites were observed in the facial nerve nucleus area on the injured side in the three groups (Fig. 6A-C). As shown in Fig. 6D, the number of Fluorogold-labeled cells in the ANA + cells group was slightly less than that in the autograft group ($P > 0.05$), but obviously more than that in the ANA group ($P < 0.05$).

3.4 Histology of the regenerated nerve

The regenerated nerves were light red in color, and microvessels could be observed on the surface of the epineuria. There was no swelling or neuroma at the proximal and distal anastomoses. The diameter of the regenerated segments was slightly thinner than the proximal and distal segments of the facial nerve defects.

The positive expression of CD31 reflected the vascular endothelial cells in the regenerated nerve segments (Fig. 7A, 7D and 7G). S100 was one of the markers of Schwann cells, which related to myelin formation of peripheral nerves (Fig. 7B, 7E and 7H), and β-tubulin III was one of the cytoskeletal proteins secreted by Schwann cells, which provided structural support for axon growth (Fig. 7C, 7F and 7I).

As shown in Fig. 8A, CD31 immunofluorescence staining of the nerve graft segments showed that the density of neovessels in the ANA group was significantly lower than that in the other two groups ($P <$

0.05), but there was no significant difference between the ANA + cells group and the autograft group (*P*> 0.05).

Many cells positively expressed S100 and β-tubulin III in all groups at 14 weeks post-surgery, respectively. The mean gray value of S100 and β-tubulin III in the ANA group was lower than the other two groups (*P*< 0.05), and the result in the ANA + cells group was similar to those in the autograft group (*P*< 0.05) (Fig. 8B and 8C) .

The ultra-thin sections of the regenerated nerves revealed that the regenerated nerve fibers in the ANA + cells group were clustered and those in the other two groups were scattered, and most of the myelin laminae were clear and regular in all groups (Fig. 9A-F).

The number and the diameter of the myelinated nerve fibers in the ANA group was less than the other two groups, respectively (*P*< 0.05), while the values of the two indexes in the ANA + cells group was similar to those in the autograft group (*P*> 0.05) (Fig. 10A and 10B). Additionally, the thickness of the myelin sheaths was the thinnest in the ANA group, and the thickest in the autograft group (*P*< 0.05) (Fig. 10C).

4. Discussion

Recently, acellular nerve grafts were widely used in bridging peripheral nerve defects due to their perfect extracellular matrix without immunogenic substances [29, 30], and support the migration and proliferation of the transplanted cells and autologous Schwann cells during nerve regeneration [31–33]. In this paper, we used a novel cell tracker to monitor the transplanted EPI-NCSCs within the ANAs *in vivo*. As shown in Fig. 2, CelTrac1000-labeled EPI-NCSCs were successfully detected by NIR-II optical imaging system for up to 14 weeks in a rat model. This may be the first report in the English literature to apply CelTrac1000 and NIR-II to tracking the transplanted stem cells after repairing peripheral nerve defects, which was different from rat model of sciatic nerve suture reported by Dong in 2021 [34]. Our data further confirmed the high labeling efficiency of CelTrac1000 and stable imaging capabilities of NIR-II *in vivo* in animal models [35, 36].

In the ANA + cells group, a small number of Celtrac1000-labeled EPI-NCSCs leaked from the anastomoses into the surrounding environment early after transplantation [37]. Subsequently, the exudated cells died rapidly, and CelTrac1000 was metabolized and excreted from the living body. Meanwhile, with the migration and proliferation of Celtrac1000-labeled EPI-NCSCs within the ANAs, the distribution of fluorescence signals gradually changed from scattered or irregular to columnar. In comparison, the fluorescence signals of NIR-II in the ANA group only appeared in the early postoperative period. Thus, it was reasonable to believe that the NIR-II fluorescence signals detected in the ANA + cells group from the 3rd week were only from live EPI-NCSCs [18].

It has been reported that ANAs could provide a good growth environment for stem cells or Schwann cells *in vivo* [22, 38, 39]. Additionally, studies have confirmed that chemokines secreted from the nerve stumps can not only recruit endogenous cells to assist nerve fiber regeneration, but also affect the migration

characteristics of the implanted cells [40–43]. Therefore, the shape and diameter of the signal region tended to be consistent with the regenerated nerve in the present study, which was may be closely related to the migration and proliferation of EPI-NCSCs in the ANAs.

To semiquantitatively evaluate the migration and proliferation of the transplanted EPI-NCSCs, the fluorescence area and average fluorescence intensity of the area were measured in a selected region around the interest area [18]. In the present study, the fluorescence probes are partially excreted into the micro-environment, which may lead to a decrease in the fluorescence area and total fluorescence intensity with the extension of observation time. However, the average fluorescence intensity did not decrease significantly, which may be related to the proliferation of the transplanted EPI-NCSCs *in vivo*. Whether the average fluorescence signal will gradually weaken with the further extension of observation time needs further study.

The role of EPI-NCSCs within the ANAs may be verified by functional assessment and histological detection. Firstly, the recovery of the vibrissa movement, the onset latency and amplitude of CMAPs in the ANA + cells group was better than those in the ANA group ($P < 0.05$), and similar to those in the autograft group ($P > 0.05$). Secondly, the number of Fluorogold-labeled motoneurons in the ANA group was less than that in the other two groups ($P < 0.05$). Thirdly, morphological examination of the regenerative nerves showed that the density of the neovessels, the number and the diameter of the myelinated nerve fibers, the thickness of the myelin sheaths in the ANA group was significantly worse than those in the other two groups ($P < 0.05$). However, histological features of the regenerated nerves in the ANA + cells group were similar to those in the autograft group ($P > 0.05$), except for significant difference in the myelin thickness ($P < 0.05$). These results indicated that when repairing long-distance facial nerve defects in rats, the neural functional and morphological recovery in the ANA laden with EPI-NCSCs group were superior to cell-free acellular scaffolds [32, 44, 45].

The results of the present study suggested that the molecular mechanism of EPI-NCSCs combined with ANAs to promote facial nerve regeneration may involve multiple factors such as cell replacement, growth factor production, and micro-environment construction [46–48]. By tracking and testing the *in vivo* properties of EPI-NCSCs, we had a preliminary knowledge of the interaction between EPI-NCSCs and ANAs, laying the foundation for optimizing stem cell-based therapeutic regimens. However, further studies are still needed regarding the regulatory effects of exogenous EPI-NCSCs on recipient tissue and cells.

5. Conclusion

The migration map of local CelTrac1000-labeled EPI-NCSCs were successfully monitored by the NIR-II fluorescence imaging system when EPI-NCSCs within the ANAs were applied to treat rat facial nerve defects. Additionally, EPI-NCSCs promoted the ANAs to repair facial nerve defects in a small animal model.

Abbreviations

NIR-II	second near-infrared window
HSA	human serum albumin
Tat	transcriptional activator protein
EPI-NCSCs	epidermal neural crest stem cells
ANAs	acellular nerve allografts
SD	Sprague-Dawley
DMEM/F12	Dulbecco's Modified Eagle Media/Ham's F 12 nutrient medium
FBS	fetal bovine serum
ITS	Insulin-Transferrin-Selenium
EGF	epidermal growth factor
CMAPs	compound muscle action potentials
S100	soluble protein-100

Declarations

Ethics approval and consent to participate:

All animal experiments were conducted according to the National Institutes of Health Guide for the Care and Use of Laboratory Animals, and the project "Experimental Study on Repairing Facial Nerve Long-Distance Defects by Acellular Nerve Grafts Combined with Hair Follicle Epidermal Neural Crest Stem Cell-Derived Schwann Cells" was approved by the Laboratory Animal Management Committee and the Ethics Review Committee of Nanjing Medical University Affiliated with Wuxi No 2 People's Hospital (approval No. 2018-D-1) on March 15, 2018.

Consent for publication:

Not applicable.

Availability of data and materials:

The data sets generated and analyzed during the current study are not publicly available, but are available from the first author (SL) on reasonable request.

Competing interests:

Authors' contributions:

SL, **JZ**, **LT** and **QL**:experiment implementation; **SL** and **GZ**:paper writing; **GZ**: obtaining funding, protocol design, data analysis and figure preparation, review and editing.All authors read and approved the final manuscript.

References

1. Fujii Y, Hatori A, Chikazu D, Ogasawara T. Application of Dental Pulp Stem Cells for Bone and Neural Tissue Regeneration in Oral and Maxillofacial Region. Stem Cells Int. 2023;2023:2026572.

2. Son D, Zheng J, Kim IY, Kang PJ, Park K, Priscilla L, Hong W, Yoon BS, Park G, Yoo JE, Song G, Lee JB, You S. Human induced neural stem cells support functional recovery in spinal cord injury models. Exp Mol Med. 2023;55(6):1182-1192.

3. Gu J, Xu H, Xu YP, Liu HH, Lang JT, Chen XP, Xu WH, Deng Y, Fan JP. Olfactory ensheathing cells promote nerve regeneration and functional recovery after facial nerve defects. Neural Regen Res. 2019;14(1):124-131.

4. Kruminis-Kaszkiel E, Osowski A, Bejer-Oleńska E, Dziekoński M, Wojtkiewicz J. Differentiation of Human Mesenchymal Stem Cells from Wharton's Jelly Towards Neural Stem Cells Using A Feasible and Repeatable Protocol. Cells. 2020;9(3):739.

5. Xue W, Shi W, Kuss M, Kong Y, Alimi OA, Wang H, DiMaio DJ, Yu C, Duan B. A Dual-network Nerve Adhesive with Enhanced Adhesion Strength Promotes Transected Peripheral Nerve Repair. Adv Funct Mater. 2023;33(2):2209971.

6. Hong KH, Kim YM, Song SC. Fine-Tunable and Injectable 3D Hydrogel for On-Demand Stem Cell Niche. Adv Sci (Weinh). 2019;6(17):1900597.

7. Zhou S, Lei Y, Wang P, Chen J, Zeng L, Qu T, Maldonado M, Huang J, Han T, Wen Z, Tian E, Meng X, Zhong Y, Gu J. Human Umbilical Cord Mesenchymal Stem Cells Encapsulated with Pluronic F-127

Enhance the Regeneration and Angiogenesis of Thin Endometrium in Rat via Local IL-1β Stimulation. Stem Cells Int. 2022;2022:7819234.

8. Lan M, Zhu L, Wang Y, Shen D, Fang K, Liu Y, Peng Y, Qiao B, Guo Y. Multifunctional nanobubbles carrying indocyanine green and paclitaxel for molecular imaging and the treatment of prostate cancer. J Nanobiotechnology. 2020;18(1):121.

9. Ribot EJ, Miraux S, Konsman JP, Bouchaud V, Pourtau L, Delville MH, Franconi JM, Thiaudière E, Voisin PJ. In vivo MR tracking of therapeutic microglia to a human glioma model. NMR Biomed. 2011;24(10):1361-1368.

10. Kircher MF, Allport JR, Graves EE, Love V, Josephson L, Lichtman AH, Weissleder R. In vivo high resolution three-dimensional imaging of antigen-specific cytotoxic T-lymphocyte trafficking to tumors. Cancer Res. 2003;63(20):6838-6846.

11. Zhang SJ, Wu JC. Comparison of imaging techniques for tracking cardiac stem cell therapy. J Nucl Med. 2007;48(12):1916-1919.

12. Lu L, Li B, Ding S, Fan Y, Wang S, Sun C, Zhao M, Zhao CX, Zhang F. NIR-II bioluminescence for in vivo high contrast imaging and in situ ATP-mediated metastases tracing. Nat Commun. 2020;11(1):4192.

13. Rbia N, Bulstra LF, Thaler R, Hovius SER, van Wijnen AJ, Shin AY. In Vivo Survival of Mesenchymal Stromal Cell-Enhanced Decellularized Nerve Grafts for Segmental Peripheral Nerve Reconstruction. J Hand Surg Am. 2019;44(6):514.e1-514.e11.

14. Tong Z, Deng Z, Wang KK. Ultra-sensitive single pixel bioluminescence tomography for in vivo cell tracking. Biomed Opt. 2022;2022:JTu3A.45.

15. Li H, Gan X, Pan L, Zhang Y, Hu X, Wang Z. EGF/bFGF promotes survival, migration and differentiation into neurons of GFP-labeled rhesus monkey neural stem cells xenografted into the rat brain. Biochem Biophys Res Commun. 2022;620:76-82.

16. Wan H, Du H, Wang F, Dai H. Molecular imaging in the second near-infrared window. Adv Funct Mater. 2019;29(25):1900566.

17. Wu M, Li X, Mu X, Zhang X, Wang H, Zhang XD. Multimodal molecular imaging in the second near-infrared window. Nanomedicine (Lond). 2022;17(21):1585-1606.

18. Chen H, Yang H, Zhang C, Chen S, Zhao X, Zhu M, Wang Z, Wang Y, Wo HT, Li K, Cheng Z. Differential Responses of Transplanted Stem Cells to Diseased Environment Unveiled by a Molecular NIR-II Cell Tracker. Research (Wash D C). 2021;2021:9798580.

19. Yang L, Conley BM, Yoon J, Rathnam C, Pongkulapa T, Conklin B, Hou Y, Lee KB. High-Content Screening and Analysis of Stem Cell-Derived Neural Interfaces Using a Combinatorial Nanotechnology and Machine Learning Approach. Research (Wash D C). 2022;2022:9784273.

20. Zhang L, Li B, Liu B, Dong Z. Co-transplantation of Epidermal Neural Crest Stem Cells and Olfactory Ensheathing Cells Repairs Sciatic Nerve Defects in Rats. Front Cell Neurosci. 2019;13:253.

21. Mousavi SM, Akbarpour B, Karimi-Haghighi S, Pandamooz S, Belém-Filho IJA, Masís-Calvo M, Salimi H, Lashanizadegan R, Pouramini A, Owjfard M, Hooshmandi E, Bayat M, Zafarmand SS, Dianatpour

M, Salehi MS, Borhani-Haghighi A. Therapeutic potential of hair follicle-derived stem cell intranasal transplantation in a rat model of ischemic stroke. BMC Neurosci. 2022;23(1):47.

22. Pan Y, Tang L, Dong S, Xu M, Li Q, Zhu G. Exosomes from Hair Follicle Epidermal Neural Crest Stem Cells Promote Acellular Nerve Allografts to Bridge Rat Facial Nerve Defects. Stem Cells Dev. 2023;32(1-2):1-11.

23. Karimi-Haghighi S, Pandamooz S, Jurek B, Fattahi S, Safari A, Azarpira N, Dianatpour M, Hooshmandi E, Bayat M, Owjfard M, Zafarmand SS, Mostaghel M, Mousavi SM, Jashire Nezhad N, Eraghi V, Fadakar N, Rahimi Jaberi A, Garcia-Esperon C, Spratt N, Levi C, Salehi MS, Borhani-Haghighi A. From Hair to the Brain: The Short-Term Therapeutic Potential of Human Hair Follicle-Derived Stem Cells and Their Conditioned Medium in a Rat Model of Stroke. Mol Neurobiol. 2023;60(5):2587-2601.

24. Zhu G, Lou W. Regeneration of facial nerve defects with xenogeneic acellular nerve grafts in a rat model. Head Neck. 2014;36(4):481-486.

25. Zhu GC, Xiao DJ, Zhu BW, Xiao Y. Repairing whole facial nerve defects with xenogeneic acellular nerve grafts in rhesus monkeys. Neural Regen Res. 2022;17(5):1131-1137.

26. Attiah MA, de Vries J, Richardson AG, Lucas TH. A Rodent Model of Dynamic Facial Reanimation Using Functional Electrical Stimulation. Front Neurosci. 2017;11:193.

27. Ando M, Ikeguchi R, Aoyama T, Tanaka M, Noguchi T, Miyazaki Y, Akieda S, Nakayama K, Matsuda S. Long-Term Outcome of Sciatic Nerve Regeneration Using Bio3D Conduit Fabricated from Human Fibroblasts in a Rat Sciatic Nerve Model. Cell Transplant. 2021;30:9636897211021357.

28. Wang Z, Huang J, Liu C, Liu L, Shen Y, Shen C, Liu C. BAF45D Downregulation in Spinal Cord Ependymal Cells Following Spinal Cord Injury in Adult Rats and Its Potential Role in the Development of Neuronal Lesions. Front Neurosci. 2019;13:1151.

29. Robinson J, Fisher D. Facial Nerve Reconstruction Using Acellular Nerve Allograft. J Craniofac Surg. 2022;33(4):e413-e414.

30. Hu M, Xiao H, Niu Y, Liu H, Zhang L. Long-Term Follow-Up of the Repair of the Multiple-Branch Facial Nerve Defect Using Acellular Nerve Allograft. J Oral Maxillofac Surg. 2016;74(1):218.e1-e11.

31. Pan J, Zhao M, Yi X, Tao J, Li S, Jiang Z, Cheng B, Yuan H, Zhang F. Acellular nerve grafts supplemented with induced pluripotent stem cell-derived exosomes promote peripheral nerve reconstruction and motor function recovery. Bioact Mater. 2021;15:272-287.

32. Liang J, Luo L, Xiang F, Lan SL, Tan XQ, Gu H, Yang KW, Ye J, Tang L, Yang Y. Acellular nerve grafts with bone marrow mesenchymal stem cells/Schwann cells for sciatic nerve regeneration in rats: a meta-analysis. J Neurosurg Sci. 2023;67(2):241-247.

33. Chow L, McGrath S, de Arruda Saldanha C, Whalen LR, Packer R, Dow S. Generation of Neural Progenitor Cells From Canine Induced Pluripotent Stem Cells and Preliminary Safety Test in Dogs With Spontaneous Spinal Cord Injuries. Front Vet Sci. 2020;7:575938.

34. Dong S, Feng S, Chen Y, Chen M, Yang Y, Zhang J, Li H, Li X, Ji L, Yang X, Hao Y, Chen J, Wo Y. Nerve Suture Combined With ADSCs Injection Under Real-Time and Dynamic NIR-II Fluorescence Imaging in Peripheral Nerve Regeneration in vivo. Front Chem. 2021;9:676928.

35. Yang L, Conley BM, Yoon J, Rathnam C, Pongkulapa T, Conklin B, Hou Y, Lee KB. High-Content Screening and Analysis of Stem Cell-Derived Neural Interfaces Using a Combinatorial Nanotechnology and Machine Learning Approach. Research (Wash D C). 2022;2022:9784273.

36. Rogozinski N, Yanez A, Bhoi R, Lee MY, Yang H. Current methods for fabricating 3D cardiac engineered constructs. iScience. 2022;25(5):104330.

37. Li Y, Takanari K, Nakamura R, Kambe M, Ebisawa K, Oishi M, Kamei Y. Artificial PGA/Collagen-based Bilayer Conduit in Short Gap Interposition Setting Provides Comparable Regenerative Potential to Direct Suture. Plast Reconstr Surg Glob Open. 2023;11(3):e4875.

38. Liang J, Luo L, Xiang F, Lan SL, Tan XQ, Gu H, Yang KW, Ye J, Tang L, Yang Y. Acellular nerve grafts with bone marrow mesenchymal stem cells/Schwann cells for sciatic nerve regeneration in rats: a meta-analysis. J Neurosurg Sci. 2023;67(2):241-247.

39. Ma X, Elsner E, Cai J, Smith TL, Li Z. Peripheral Nerve Regeneration with Acellular Nerve Allografts Seeded with Amniotic Fluid-Derived Stem Cells. Stem Cells Int. 2022;2022:5240204.

40. Pandamooz S, Jurek B, Dianatpour M, Haerteis S, Limm K, Oefner PJ, Dargahi L, Borhani-Haghighi A, Miyan JA, Salehi MS. The beneficial effects of chick embryo extract preconditioning on hair follicle stem cells: A promising strategy to generate Schwann cells. Cell Prolif. 2023;56(7):e13397.

41. Vasyliev RG, Gubar OS, Gordiienko IM, Litvinova LS, Rodnichenko AE, Shupletsova VV, Zlatska AV, Yurova KA, Todosenko NM, Khadzhynova VE, Shulha MV, Novikova SN, Zubov DO. Comparative Analysis of Biological Properties of Large-Scale Expanded Adult Neural Crest-Derived Stem Cells Isolated from Human Hair Follicle and Skin Dermis. Stem Cells Int. 2019;2019:9640790.

42. Guo YC, Chiu YH, Chen CP, Wang HS. Interleukin-1β induces CXCR3-mediated chemotaxis to promote umbilical cord mesenchymal stem cell transendothelial migration. Stem Cell Res Ther. 2018;9(1):281.

43. Qian Y, Yao Z, Wang X, Cheng Y, Fang Z, Yuan WE, Fan C, Ouyang Y. (-)-Epigallocatechin gallate-loaded polycaprolactone scaffolds fabricated using a 3D integrated moulding method alleviate immune stress and induce neurogenesis. Cell Prolif. 2020;53(1):e12730.

44. Choi SJ, Park SY, Shin YH, Heo SH, Kim KH, Lee HI, Kim JK. Mesenchymal Stem Cells Derived from Wharton's Jelly Can Differentiate into Schwann Cell-Like Cells and Promote Peripheral Nerve Regeneration in Acellular Nerve Grafts. Tissue Eng Regen Med. 2021;18(3):467-478.

45. Bedar M, Saffari TM, Johnson AJ, Shin AY. The effect of mesenchymal stem cells and surgical angiogenesis on immune response and revascularization of acellular nerve allografts in a rat sciatic defect model. J Plast Reconstr Aesthet Surg. 2022;75(8):2809-2820.

46. Li Y, Yao D, Zhang J, Liu B, Zhang L, Feng H, Li B. The Effects of Epidermal Neural Crest Stem Cells on Local Inflammation Microenvironment in the Defected Sciatic Nerve of Rats. Front Mol Neurosci. 2017;10:133.

47. Lin H, Liu F, Zhang C, Zhang Z, Kong Z, Zhang X, Hoffman RM. Characterization of nerve conduits seeded with neurons and Schwann cells derived from hair follicle neural crest stem cells. Tissue Eng Part A. 2011;17(13-14):1691-1698.

48. Tang N, Wang X, Zhu J, Sun K, Li S, Tao K. Labelling stem cells with a nanoprobe for evaluating the homing behaviour in facial nerve injury repair. Biomater Sci. 2022;10(3):808-818.
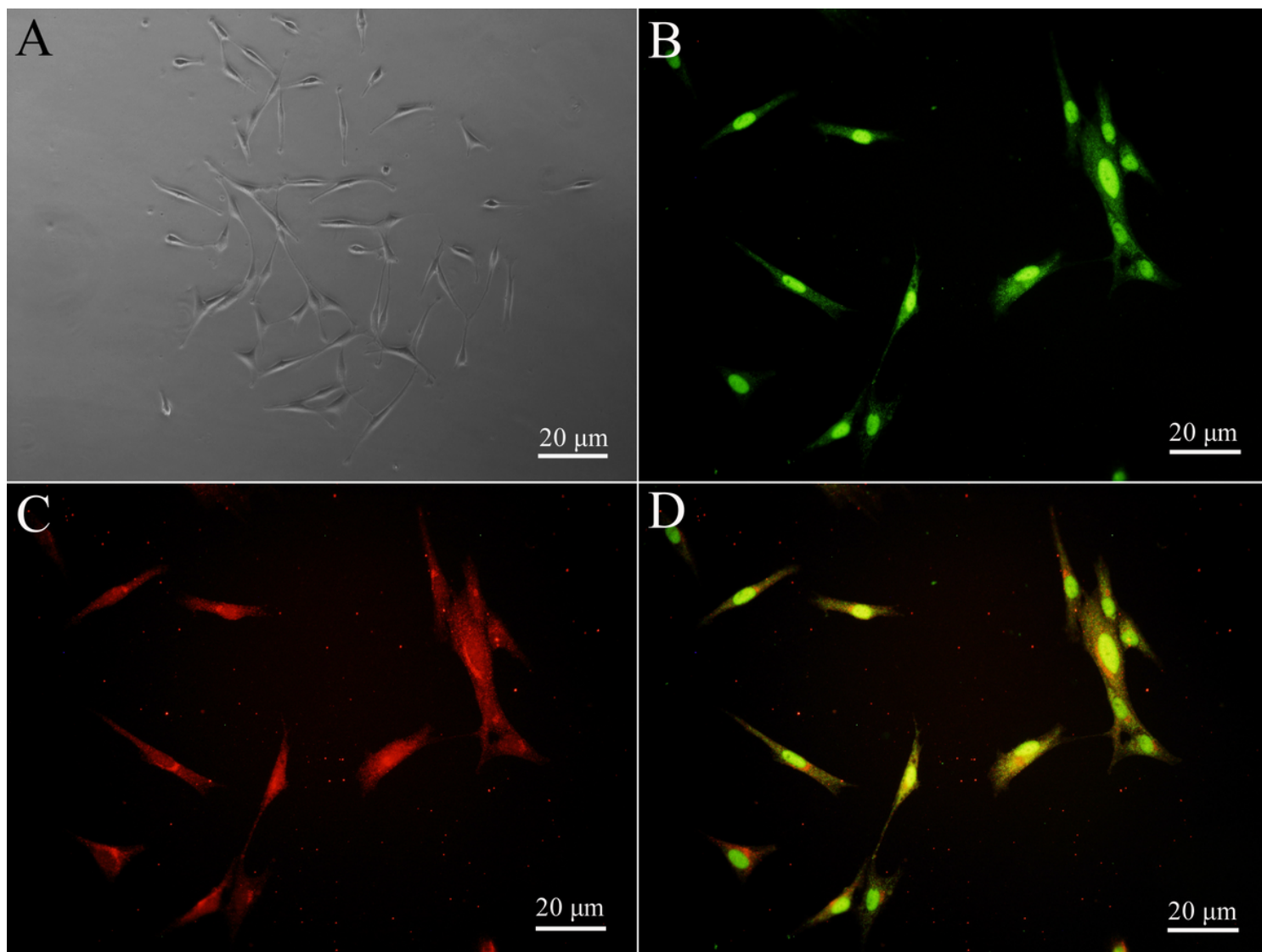
Figures

Figure 1

Culture and identification of hair follicle epidermal neural crest stem cells. The spindle-shaped cells were scattered at the bottom of the plates (A), and cells were positively expressed for SOX10 and Nestin (B: SOX10; C: Nestin; D: merged.).
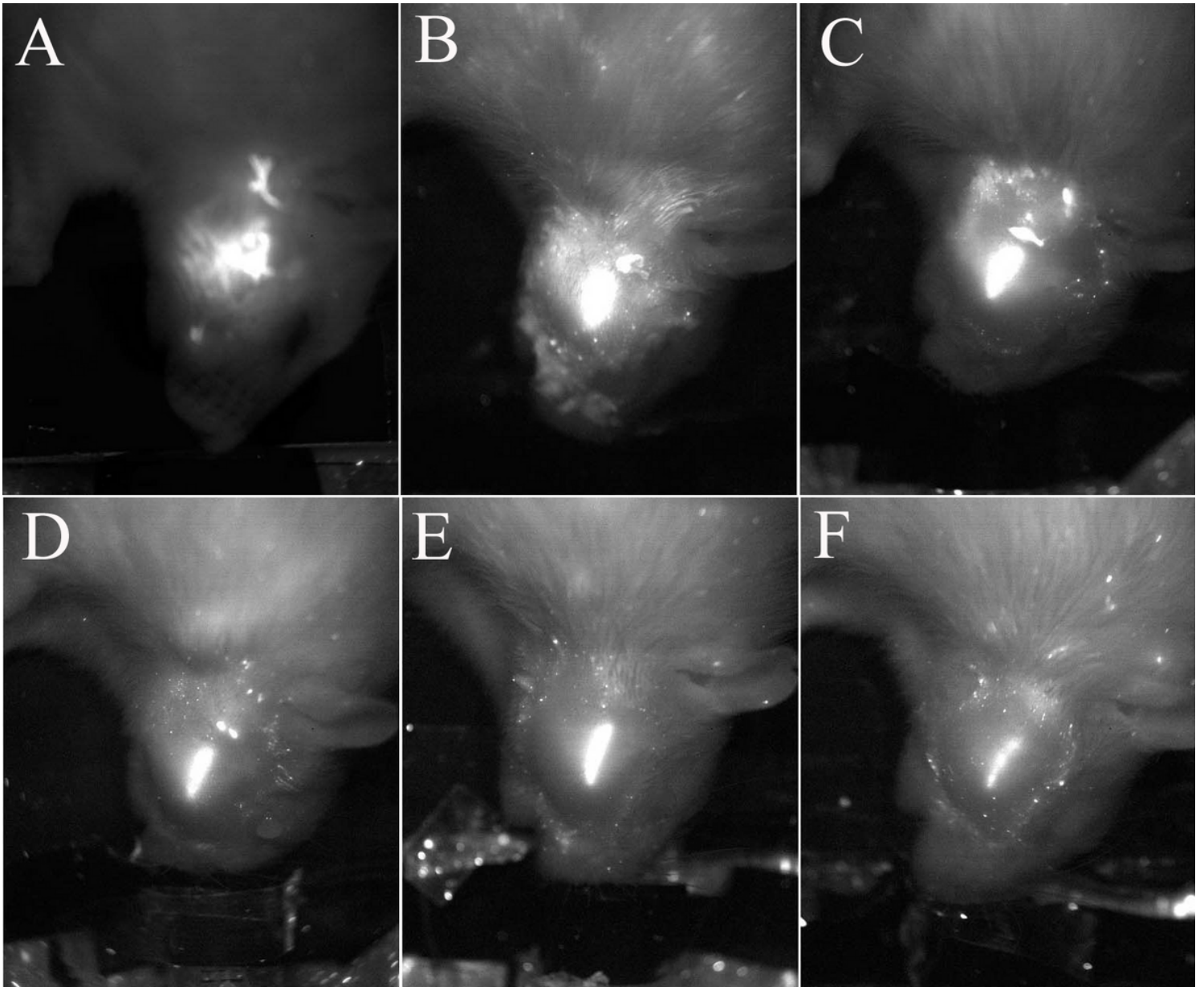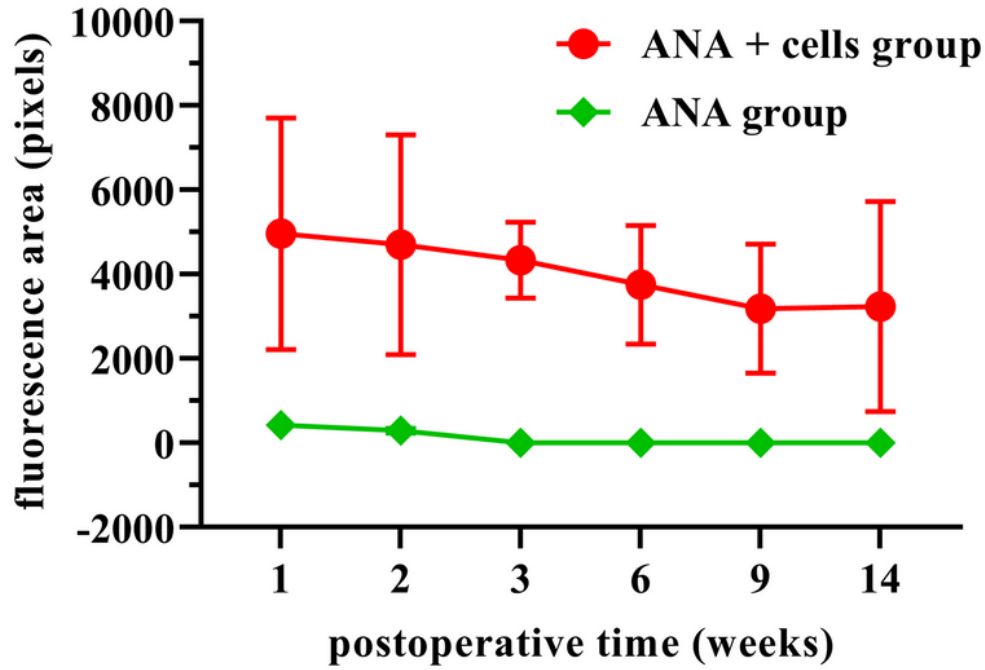
Figure 2

NIR-II fluorescence images monitored CelTrac1000-labeled EPI-NCSCs with acellular nerve allograft in repairing facial nerve defects. A: 1 week; B: 2 weeks; C: 3 weeks; D: 6 weeks; E: 9 weeks; F: 14 weeks.
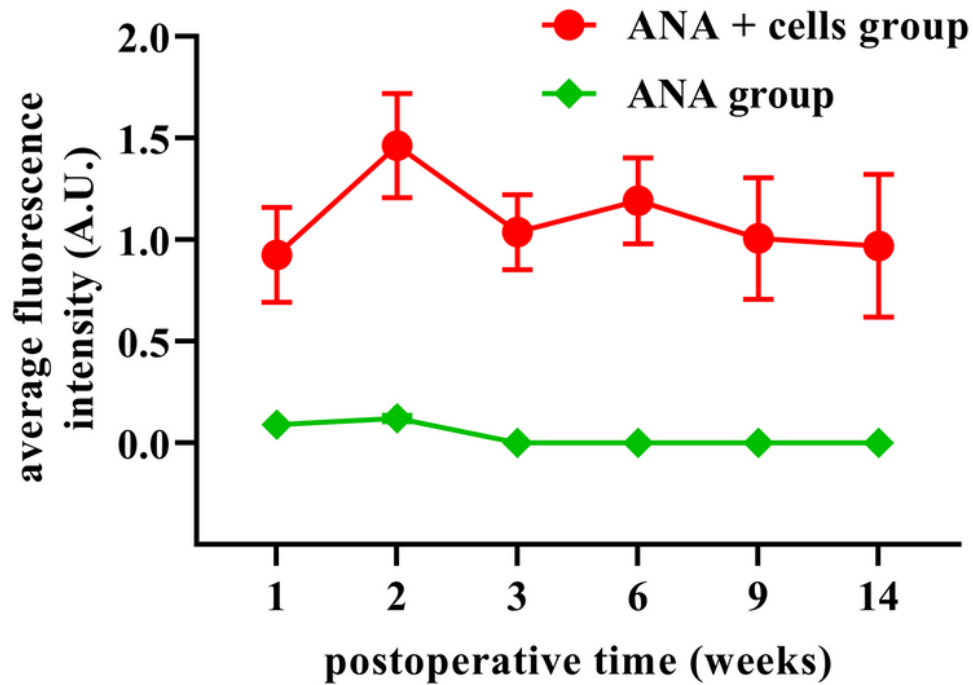
Figure 3

Semiquantitative analysis of the second near-infrared window fluorescence images. The fluorescence area (A) and the average fluorescence intensity of the area (B) in the ANA + cells group and the ANA group. ANA: acellular nerve allograft.
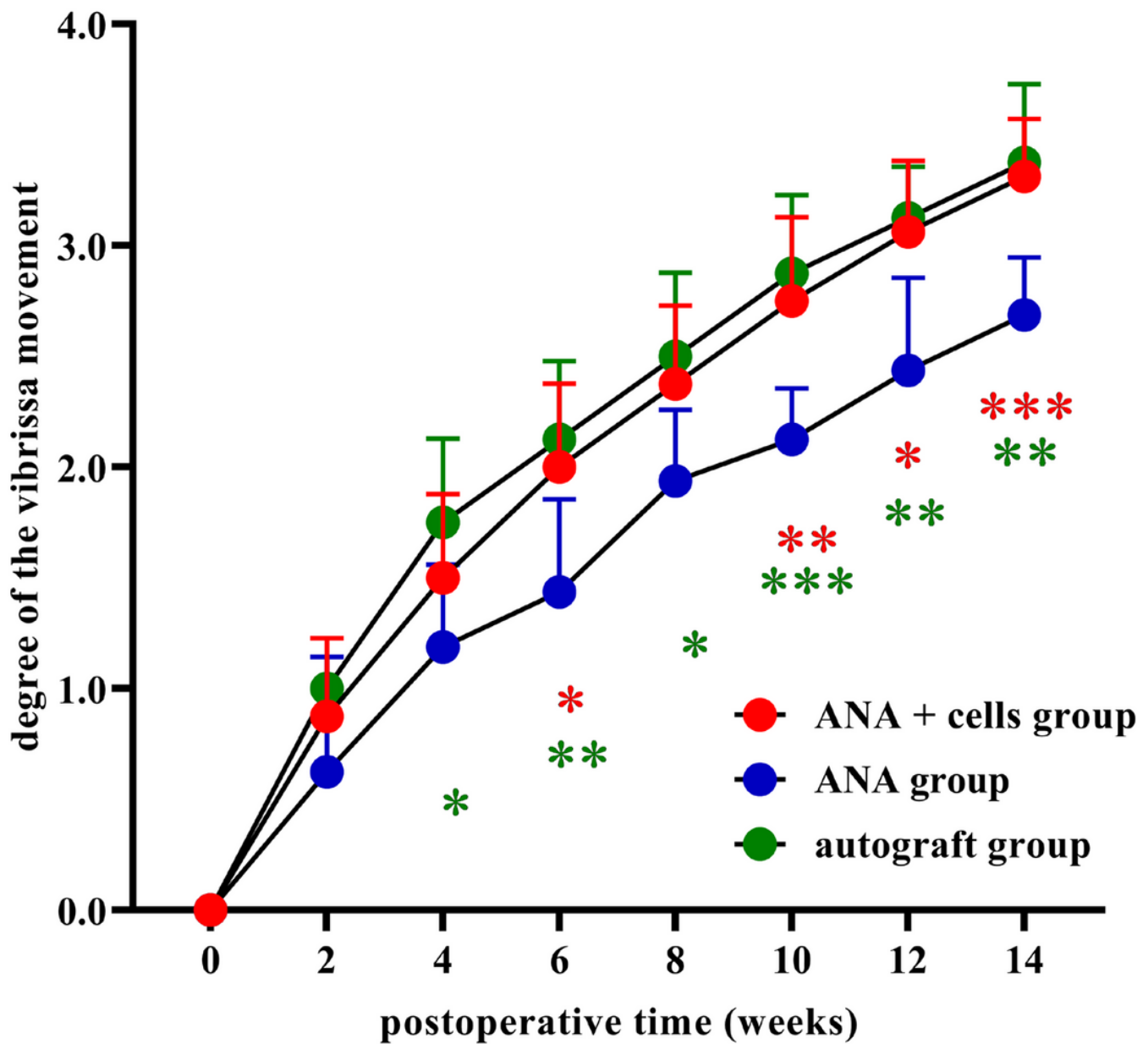
Figure 4

The degree of the vibrissa movement on the injured side. Red and green color asterisk meant that the value of the ANA group was compared with that of the ANA + cells group and the autograft group, respectively. ANA: acellular nerve allograft. * $P < 0.05$, ** $P < 0.01$, and *** $P < 0.001$.
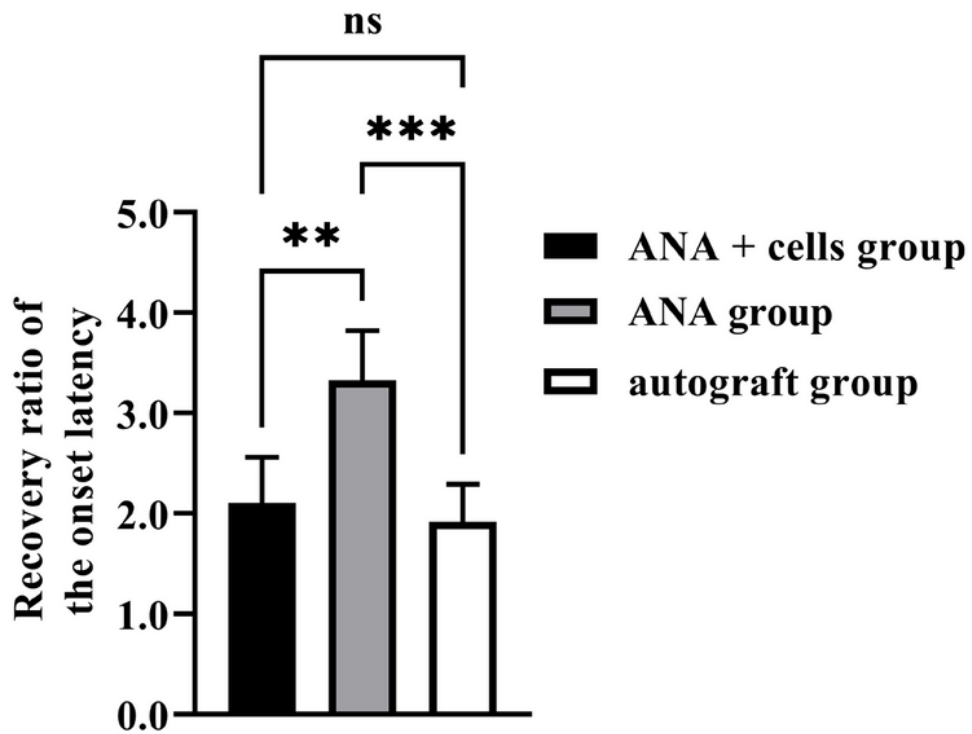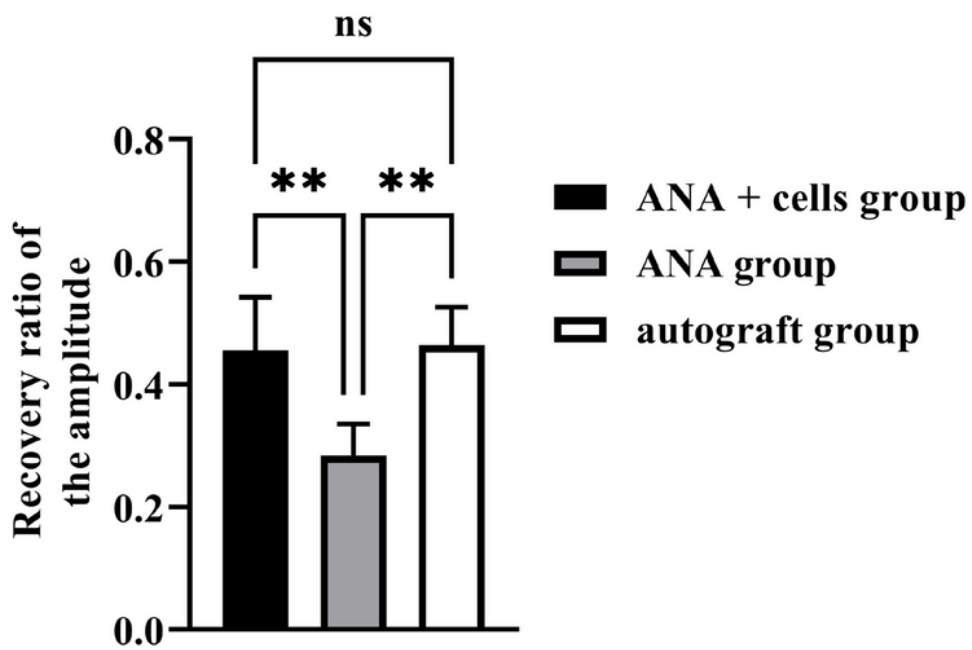
Figure 5

The recovery ratio of the compound muscle action potentials. A: the recovery ratio of the onset latency; B: the recovery ratio of the amplitude. ANA: acellular nerve allograft. ** $P< 0.01$, *** $P< 0.001$, and ns: no significance.
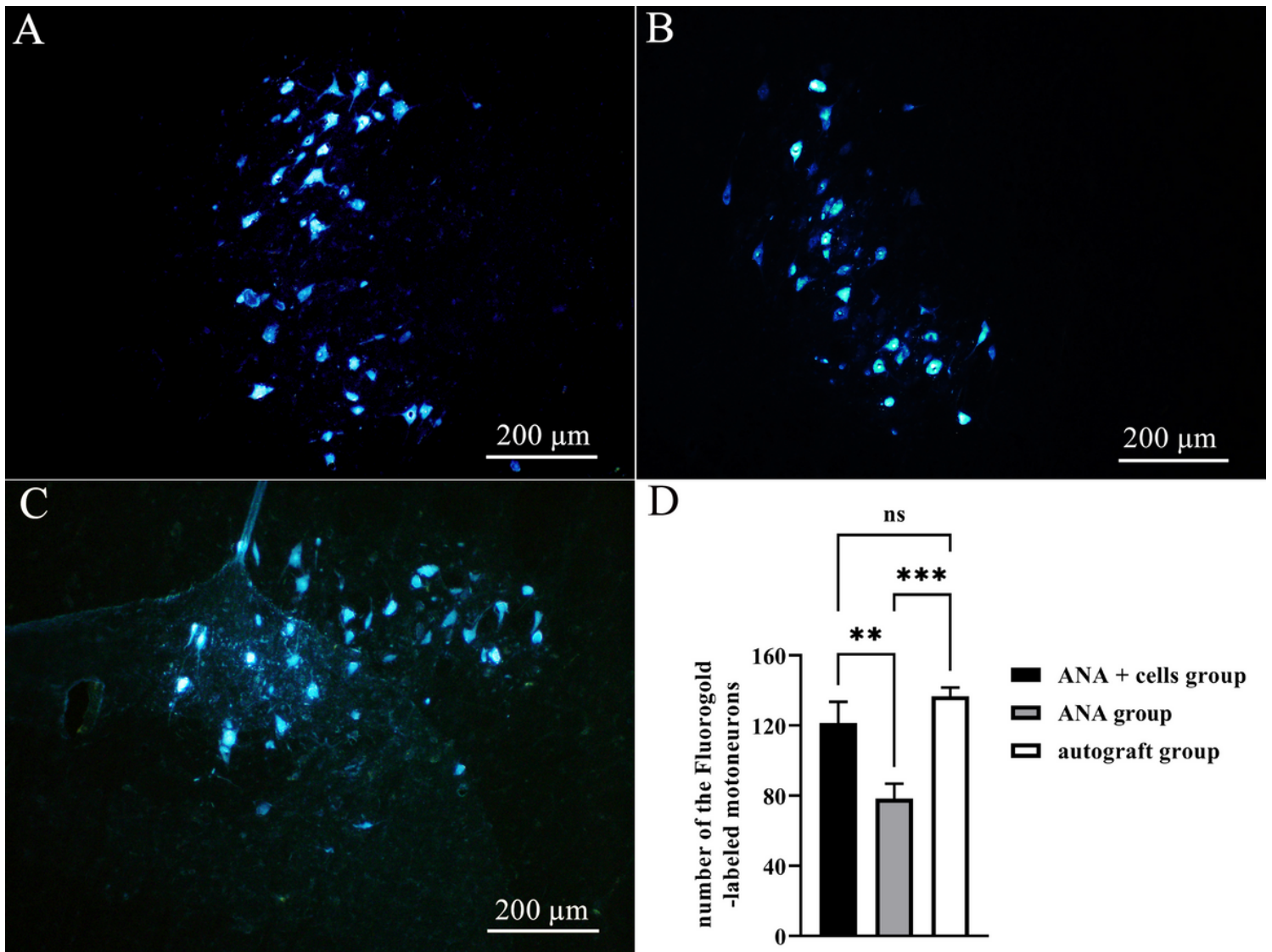
Figure 6

Images of the Fluorogold-labeled facial motoneurons on the injured side. A: ANA + cells group; B: ANA group; C: autograft group; D: comparis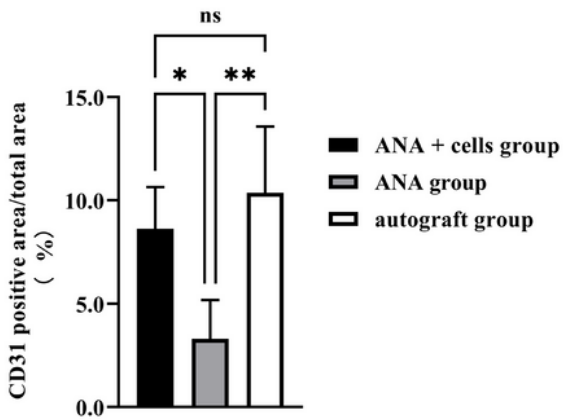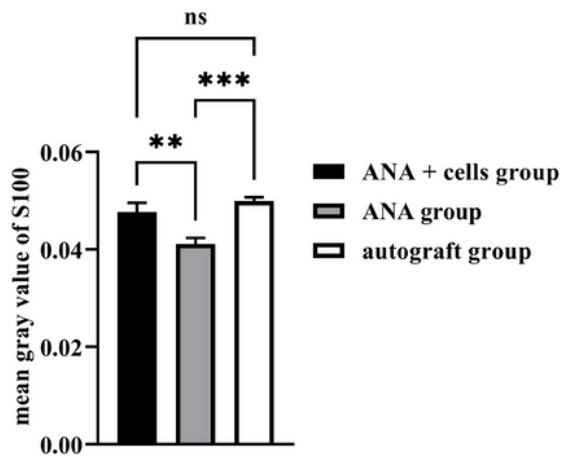on of the labeled cell number between the three groups. ANA: acellular nerve allograft. ** $P< 0.01$, *** $P< 0.001$, and ns: no significance.
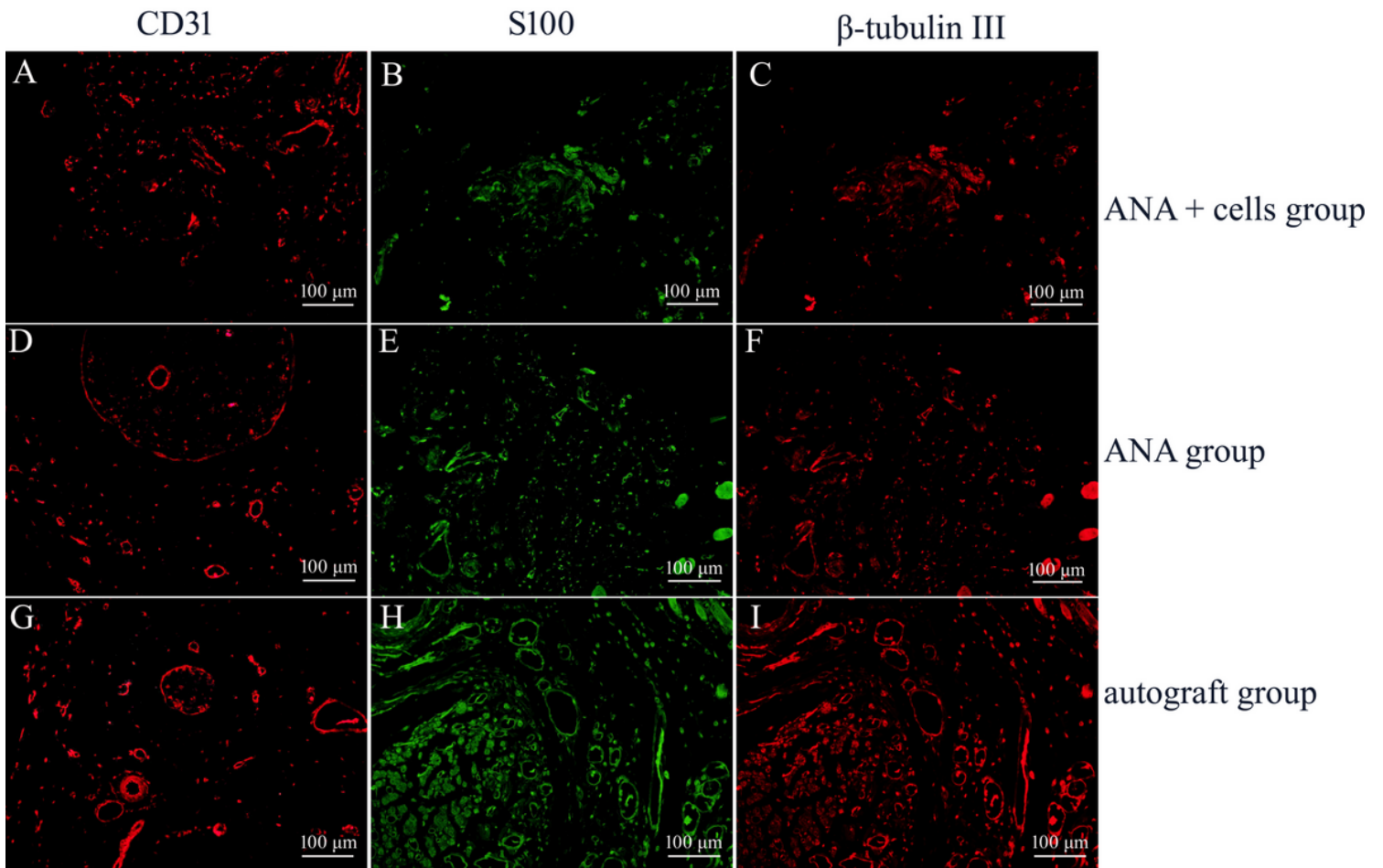
Figure 7

Immunofluorescence staining of CD31, S100 and β-tubulin III of the regenerated nerves. ANA: acellular nerve allograft.
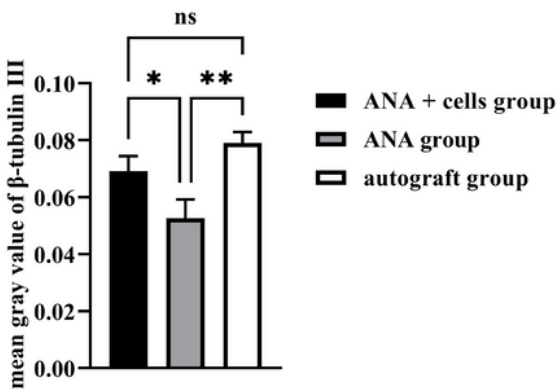
Figure 8

Comparison of the immunofluorescence staining results between the three groups. A: the CD31 positive area/total area; B: the mean gray value of S100; C: the mean gray value of β-tubulin III. ANA: acellular nerve allograft. * $P < 0.05$, ** $P < 0.01$, *** $P < 0.001$, and ns: no significance.
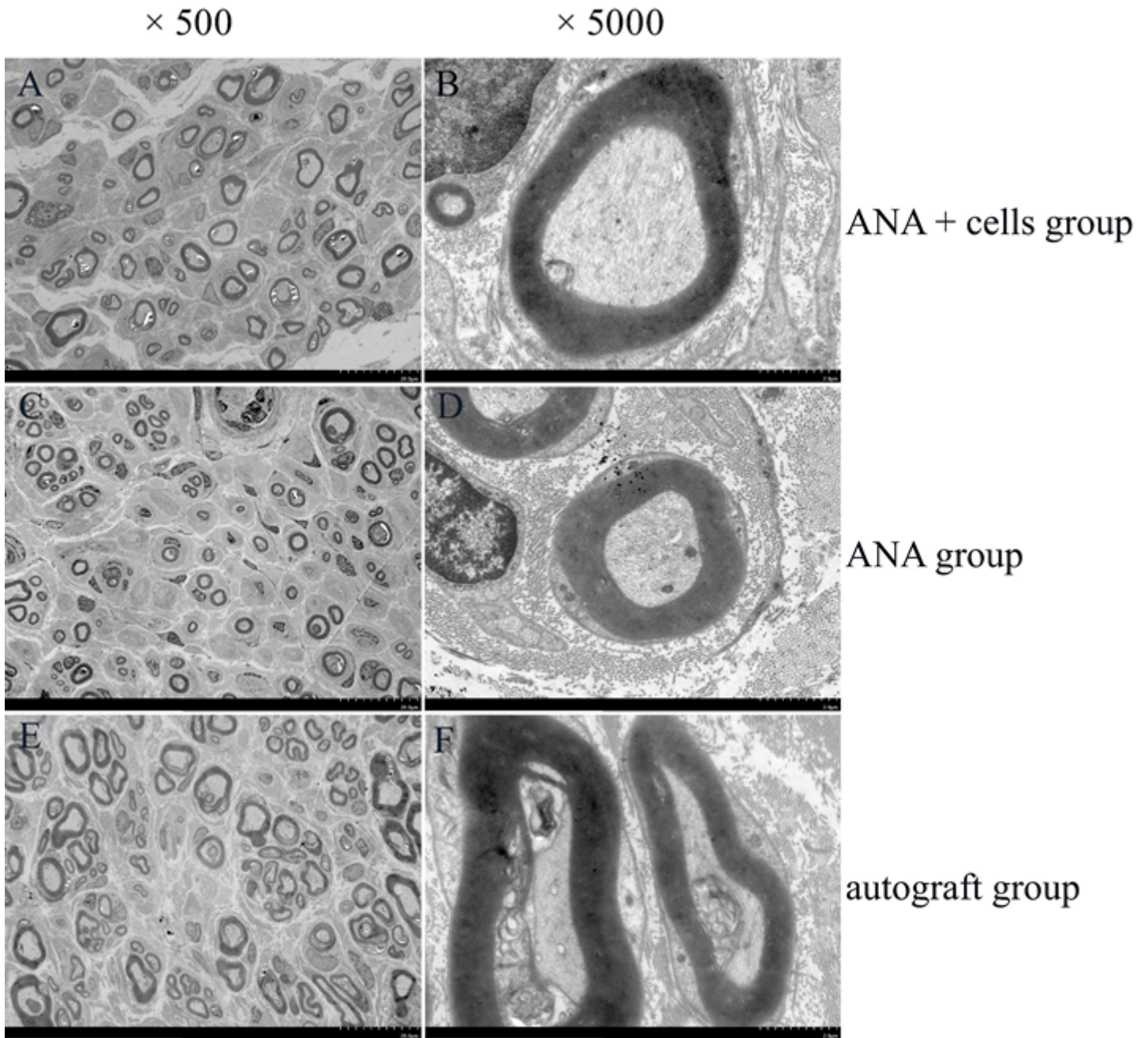
Figure 9

Transmission electron micrographs of the regenerated nerves. The regenerated nerve fibers were in scattered shapein the ANA + cells group (A, B) and ANA group (C, D), and in clustered shape in autograft group (E, F). Most of the myelin laminae were clear and regular in all groups. ANA: acellular nerve allograft.
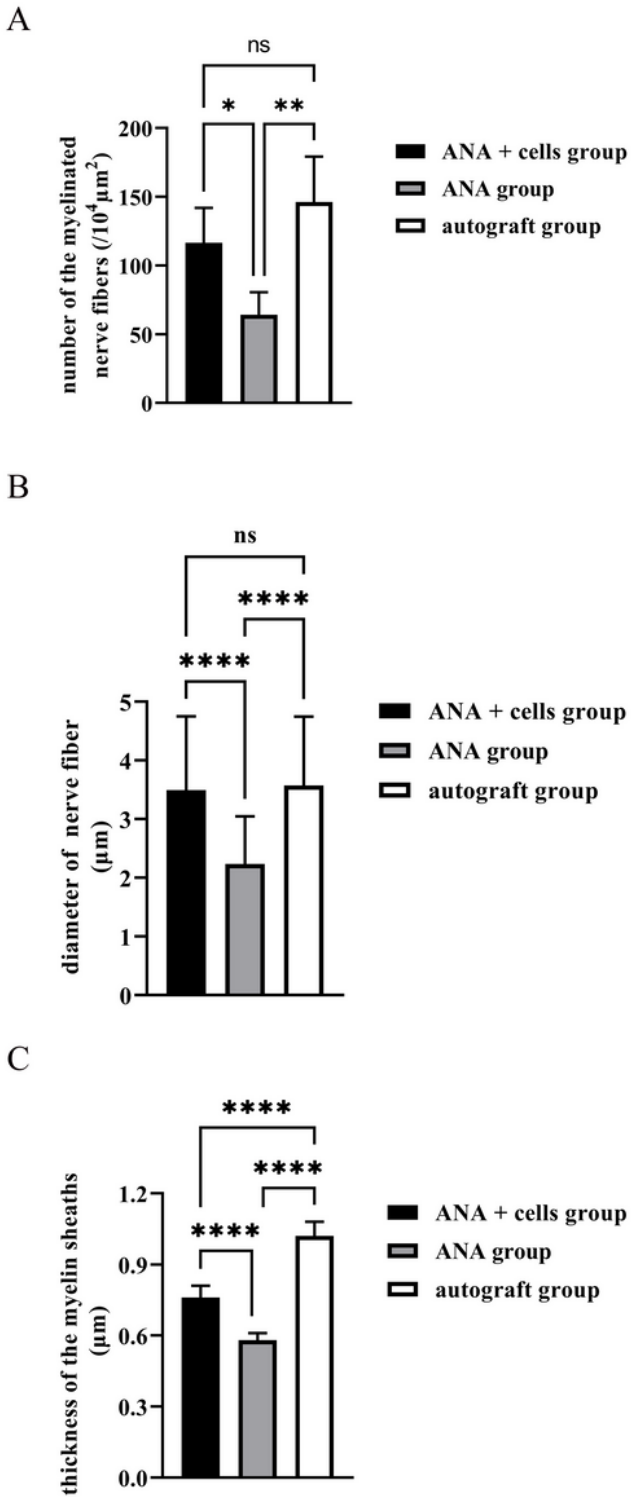
Figure 10

Comparison of indexes of the regenerated nerves in the transmission electron micrographs. A: the number of the myelinated nerve fibers; B: the diameter of the nerve fibers; C: the thickness of the myelin sheaths. ANA: acellular nerve allograft. * $P < 0.05$, ** $P < 0.01$, *** $P < 0.001$, *** $P < 0.0001$, and ns: no significance.